

Bonfigli, G., Kloker, M.J. 2003 Secondary instability of superposed steady and unsteady crossflow vortices. In *New Results in Numerical and Experimental Fluid Mechanics IV* (ed. Ch. Breitsamter & al.), NNFM 87, Springer, pp. 164-171.

Secondary instability of superposed steady and unsteady crossflow vortices

G. Bonfigli and M. Kloker

Institut für Aerodynamik und Gasdynamik,
Universität Stuttgart, Pfaffenwaldring 21, D-70550, Germany

Summary

Laminar-turbulent transition in a 3-D boundary layer under controlled simultaneous forcing of unstable steady and unsteady crossflow waves is investigated by means of direct numerical simulations. The flow configuration reproduces the accelerated 3-D flat-plate boundary layer of the "Querströmungsprinzipexperiment" of the DLR-Göttingen [1]. The superposition of high-amplitude steady and unsteady waves induces a spanwise and streamwise modulation of the flow, which is shown to trigger the laminar breakdown also in the absence of additional background disturbances. The mechanism has some similarities to the one documented for the case of purely steady vortices [6] [8]. However the interaction of the primarily perturbed waves provides both the preconditions and the forcing for such mechanism.

1 Introduction

Relevant progress has been achieved recently with respect to the final stages of transition in crossflow (CF) unstable 3-D boundary layers. First experimental results [1] [10], then theoretical works [4] [6], and finally direct numerical simulations (DNS) [8] [9] [11] showed that a strong secondary instability leads to the growth of high-frequency perturbations, which in the end trigger the onset of the turbulent regime. Furthermore, the secondary instability could be put in relation with the modulation induced by the primary vortices in the distribution of the velocity components over crosscut-planes orthogonal to their axes. However, the major part of these results is confined to fundamental scenarios where the primarily unstable modes are steady in a proper, eventually translating, galilean reference system (this is the case when the primary state is the consequence of the excitation of a single unsteady wave). Exceptions are the experimental work carried out at the DLR-Göttingen [1], where steady and unsteady unstable modes were perturbed simultaneously, and temporal DNS [11]. In the experiment high-frequency perturbations were observed but the flow was too complex to provide a conclusive picture of the breakdown mechanism, also because the theoretical model [4] [6] treating the fundamental cases might fail since its assumptions of steadiness and invariance in downstream direction are violated. Temporal DNS [11] suffer from a basic flaw in the model since initially steady modes can not be kept steady (rather the spatial wavevector is fixed).

All results presented hereafter are computed solving the vorticity-velocity formulation of the unsteady incompressible three-dimensional Navier-Stokes equations. The spatial discretization is based on a well-tested combination of 6th-order compact finite-differences (in downstream and wall-normal direction) and spanwise Fourier-spectral expansions. A 4th-order Runge-Kutta scheme is used for marching in time. Lengths are made nondimensional with $L^* = 0.1m$, velocities with $u_\infty^* = 14m/s$. The nondimensional grid steps in wall-normal and streamwise direction are $1.1 \cdot 10^{-4} \leq \Delta y \leq 4.6 \cdot 10^{-4}$ (varying depending on the wall distance) and $\Delta x = 1.3 \cdot 10^{-3}$, respectively. The number of Fourier harmonics used in spanwise direction amounts to 82. A description of the numerical procedure can be found in [8].

1.1 Baseflow and transition scenario

The baseflow reproduces the 3-D accelerated flat-plate boundary layer of the ‘‘Querströmungsprinzipexperiment’’ of the DLR-Göttingen [1] for $Q_\infty = 19m/s$. The downstream development of the most relevant boundary-layer parameters is shown in figure 1. Velocity profiles at different x -positions are also given and show everywhere the classical CF shape. Experimental data for $x = 3.0$ [1] are provided for comparison. Here and in the following, x , y and z are the downstream, the wall-normal and the spanwise coordinates, respectively, in a plate-oriented system with z parallel to the plate leading edge.

Over the whole integration domain amplification rates are maximal for CF modes with a spanwise wavelength approximately equal to $\Lambda_z^* = 12mm \approx 4 \cdot \delta_s^*$ and with frequencies in the range $0Hz \leq f^* \leq 250Hz$. Correspondingly, the nondimensional fundamental wavenumber of the spanwise Fourier expansion was set equal to $\gamma = 2\pi/\Lambda_z = 52.4$, and the frequency $f^* = 133Hz$ ($\omega_0 = 6.0$) was chosen for the unsteady disturbance. Indicating by (h, k) modes with frequency $\omega = h \cdot \omega_0$ and spanwise wavenumber $\gamma = k \cdot \gamma_0$, the modes $(0, 1)$ and $(1, 1)$ were perturbed at $x = 1.56$ by suction and blowing within a thin wall stripe parallel to the plate leading edge. The perturbation amplitudes were $A_{(0,1)} = 1.7 \cdot 10^{-3}$ and $A_{(1,1)} = 1.5 \cdot 10^{-4}$.

Figure 2 documents the downstream amplitude development for the perturbed modes. It has been shown [2] that the transition scenario varies strongly depending on the relative amplitudes of the primary modes before and after the onset of saturation. In the present simulation (hereafter called case $(0, 1) + (1, 1)$, corresponding to case R5 in [2] and to case $(0, 1) + (1, 1)$ in [5]) the CF vortex $(0, 1)$ is perturbed with larger amplitude than the CF wave $(1, 1)$ and dominates, despite weaker growth, the transitional region. At $x = 2.6$ its amplitude is nearly 10% of the local free-stream velocity u_{bse} , and further downstream it strongly influences $(1, 1)$. The amplification of both primary modes is damped by nonlinear effects. The influence of mode $(1, 1)$ on the onset of saturation, if any, is marginal. However its amplitude is not negligible ($8\% \cdot u_{bse}$) and indeed it plays a determinant role in the further development of the flow.

1.2 Transition mechanism

Up to saturation of the primary modes ($x \leq 3.4$) the flow field is still determined by the quasi-linear superposition of the disturbance fields associated with the primary modes $(0, 1)$ and $(1, 1)$ and their superharmonics. Reference simulations have been carried out where modes $(0, 1)$ or $(1, 1)$ were perturbed alone (case $(0, 1)$ and case $(1, 1)$, respectively). The resulting flow fields and the one obtained by superposing them linearly were then compared with case $(0, 1) + (1, 1)$. As figures 3a and 3b show for ω'_ξ , i. e. for the component of the perturbation vorticity parallel to the ξ -axis and nearly parallel to the axes of the most relevant vortical structures, both primary modes tend to generate stripe patterns in the vorticity distribution over every wall-parallel plane cutting the cores of the corresponding main vortices. Regions of negative ω'_ξ corresponding to the neighboring CF main vortices are separated by regions of positive shear ω'_ξ , which in case $(0, 1)$ develop into small counterrotating streamwise secondary vortices. When $(0, 1)$ and $(1, 1)$ are superimposed (fig. 3d) a checkered unsteady pattern emerges, where modulations are evident both in the direction normal and parallel to the axis of the dominating vortices $(0, 1)$. The similarity between 3c and 3d for $\xi \leq 1.0$ ($x \leq 2.85$) confirms that the vorticity modulation in case $(0, 1) + (1, 1)$ is primarily originated by linear effects.

Concentrating on case $(0, 1) + (1, 1)$, secondary instability mechanisms in the sense of the secondary linear instability theory (SLST) [4] [6] [8] [10], based on the instantaneous local crosscut flow fields, determine the flow development in the saturation region. Figure 4 shows secondary vortical structures connected to high-frequency modes I in the left column and low-frequency modes III in the right column: i) for flow fields obtained by superposing the primary state from case $(0, 1)$ with properly normed secondary modes from own SLST-computations (in conjunction with [7] and [3], figs. 4a-b); ii) for snapshots from case $(0, 1)$ under additional unsteady excitation of secondary modes in the saturation region (DNS, figs. 4c-d); iii) for the superposition of instantaneous primary states from case $(0, 1) + (1, 1)$ and the corresponding SLST secondary modes (figs. 4e-f); and iv) for snapshots from case $(0, 1) + (1, 1)$ (DNS, figs. 4g-h). The SLST-analysis for iii) has been carried out for crosscut planes of instantaneous flow fields from case $(0, 1) + (1, 1)$. Time steps and plane positions were chosen so that the perturbations finally developing into the structures of iv) crossed the considered planes at the considered time steps. The comparison of i) and ii) shows that in case $(0, 1)$ the eigenfunctions of the SLST problem provide a good approximation of the flow field also at stages where secondary vortical structures become visible and perturbation amplitudes are virtually too large for the linearity assumption to hold. It is then possible to identify instability mechanisms by considering the shape of the resulting secondary vortical structures. This can be done for case $(0, 1) + (1, 1)$ comparing iii) and iv) and one may conclude that both instability mechanisms of type I (compare figs. 4e and 4g, capital letter indicate corresponding structures) and type III (compare figs. 4f and 4h) are active in case $(0, 1) + (1, 1)$. The frequency ω and the streamwise wavenumber β_ψ of the instabilities of the secondary modes connected to the structures in iv) may be assumed equal to those of the modes generating the structures in iii) (the spatial

extension of the structures is inversely proportional to β_ψ). This gives $\omega \approx 30.0$, $\beta_\psi \approx 40.0$, for mode I and $\omega \approx 20.0$, $\beta_\psi \approx 40.0$, for mode III.

Caution is needed in applying the SLST to case $(0, 1) + (1, 1)$ since as shown in fig. 3c the flow field is strongly modulated in downstream direction, not steady in any reference system, and consequently violates the basic assumptions of the theoretical approach. However neither the generation of isolated vortical structures (see figs. 4g-h) contradicts the connection between SLST and the mechanism governing the present flow, nor does the results of fig. 5, according to which the mode-I structure of fig. 4g develops where the instantaneous velocity profiles are not particularly unstable ($2/5T$ curve) and is associated to weakly unstable frequencies ($\omega \approx 30$). On the contrary, both aspects may be explained considering the localized character of the forcing initiating the instability mechanism. Particularly relevant is the concentration of positive ω'_ξ marked as $M1$ in figure 3c and originating from the modulation induced by the superposition of the primary modes $(0, 1)$ and $(1, 1)$. Both mode I and mode III are associated to local concentrations of positive vorticity on the updraft side of the primary vortex and may be expected to be efficiently excited by vorticity concentrations in that position. Following the flow development it becomes clear that the structures of figs. 4g-h both originate from the maximum $M1$, whose positions after one and two periods of the CF wave $(1, 1)$ are marked in figure 3c by $M2$ and $M3$, respectively. The development of the two distinct ω'_ξ -maxima $M3I$ and $M3III$ (fig. 3c) from the original concentration $M1$ is the first step toward the generation of the two distinct structures and is in agreement with the known characteristics of the instability modes involved in the process. The group velocity of mode I is indeed significantly higher than that of modes III. The convection velocity of the associated structures, and before that of the local vorticity concentrations $M3I$ (connected to mode I and developing into the structure of fig. 4g) and $M3III$ (connected to mode III and developing into the structure of fig. 4h), are correspondingly different.

In conclusion it can be stated that the instability mechanism connected to modes I and III of the SLST is robust and quite insensitive to the violation of the periodicity assumption made in the theory for the downstream direction. It is driven by the interaction between the flow field generated by the primary vortex and the region of positive ω'_ξ on its updraft side and is initiated by downstream, periodical or local, modulations of the flow. The selection of the dominant instability is influenced by the character of the excitation, with the result that the observable really dominating mode is not necessarily the most amplified one. Rather the effective initial amplitudes of the various modes are important, and in the present case they decrease with increasing frequency since all unsteady perturbations are nonlinearly generated by the fundamental wave. The interaction of steady and unsteady primary modes determines the initial streamwise flow modulation and consequently the development of the transition process.

It has been verified in other DNS that, when a flat spectrum background pulse is provided, more unstable higher-frequency type-I modes prevail and generate the smaller secondary vortices documented in [8]. In case $(0, 1) + (1, 1)$ the laminar

breakdown is triggered by the mode-I structure of fig. 4g and in no case the breakdown was initiated by mode-III structures. Even in the simulation of figure 4d, where mode III was explicitly excited, the turbulent regime is initiated by the mode connected to the first superharmonic of the forcing, which is already of type I.

1.3 Comparison with the experiment

A comparison between numerical and experimental results for case $(0, 1) + (1, 1)$ is provided in figure 6 on the basis of a visualization by Lerche [5] showing the isosurfaces of the wall-normal gradient and of the second time derivative of the streamwise velocity component. The good agreement for the wall-normal gradient shows that the DNS closely reproduces the transition scenario of the experiment, while differences in the position of the high frequency perturbations are probably due to uncontrolled background unsteady perturbations in the experiment. Indeed, background noise might be there the reason for the observed relevant growth of high frequency secondary modes (the spectrum in fig. 66 of [5] shows a local maximum for $f^* \approx 2000Hz$), while in the DNS, where unsteady excitation is provided exclusively through the low frequency primary mode $(1, 1)$, modal amplitudes fall monotonously for growing frequencies.

The comparison of the temporal visualization of fig. 6 (data originate from a fixed (y, z) -plane for different time steps) and the spatial snapshot of figure 7 explains the origin of the climbing isosurfaces visible in fig. 6 for the wall-normal gradient of the downstream velocity. They follow from the profile deformation induced by the primary vortex, the climbing shape being a consequence of the streamwise flow modulation induced by the superposition of steady and unsteady primary perturbations. Finer structures, like the ones induced by the secondary instability mechanisms discussed above, are smoothed out.

The financial support by the Landesgraduiertenförderung (LGF) under grant 7631 is gratefully acknowledged.

References

- [1] H. Bippes. *Progress in Aerospace Sciences*, 35:363–412, 1999.
- [2] G. Bonfili and M. Kloker.
- [3] W. Koch. Private communications on spectral SLST-solver and eigenvalue tracking, 2001.
- [4] W. Koch, F. P. Bertolotti, A. Stolte, and S. Hein. *J. Fluid Mech.*, 406:131–174, 2000.
- [5] T. Lerche. Dissertation, Universität Göttingen, 1997.
- [6] M. R. Malik and C. L. Chang. *J. Fluid Mech.*, 268:1–36, 1994.
- [7] R. Messing. Private communications on finite-difference SLST-solver, 2002.
- [8] P. Wassermann and M. Kloker. *J. Fluid Mech.*, 456:49–84, 2002.
- [9] P. Wassermann and M. Kloker. Transition mechanisms induced by travelling crossflow vortices in a three-dimensional boundary layer. *Accepted for publication in J. Fluid Mech.*, 2002.
- [10] E. B. White, W. S. Saric, R. D. Gladden, and P. M. Gabet. AIAA 2001-0271, 2001.
- [11] T. Wintergerste and L. Kleiser. In J. Chollet, P. R. Voke, and L. Kleiser, editors, *Direct and large-eddy simulation*, volume II. Kluwer academic press, 1997.

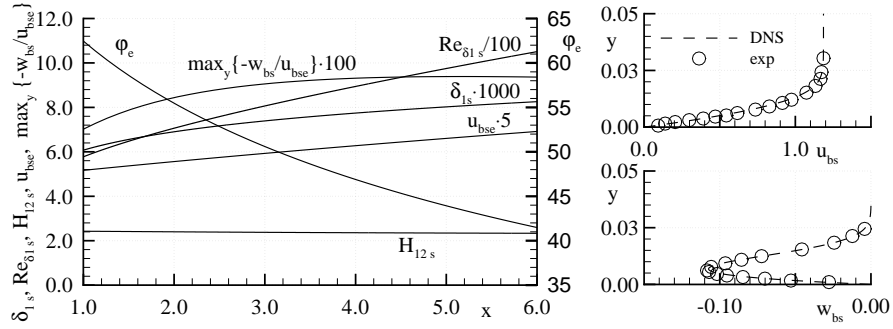


Figure 1 Parameters of the baseflow in the streamline-oriented coordinate system (local sweep angle with respect to the fixed system φ_e , displacement thickness δ_{1s} , local Reynolds number $Re_{\delta_{1s}}$, shape factor H_{12s} , maximum local CF velocity $\max_y\{-w_{bs}\}$) and velocity profiles at $x = 3.0$ for DNS and experiment.

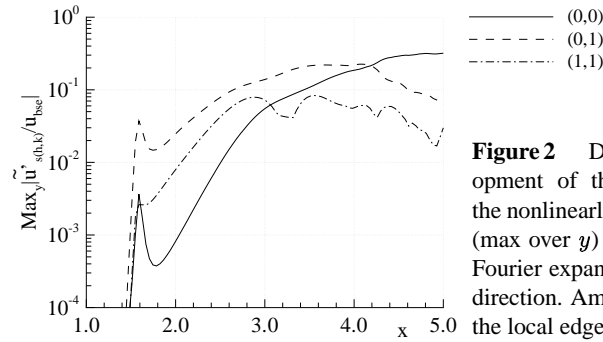


Figure 2 Downstream amplitude development of the perturbed modes and of the nonlinearly induced baseflow distortion (max over y) for case $(0, 1) + (1, 1)$ after Fourier expansion in time and in spanwise direction. Amplitudes are normalized with the local edge velocity.

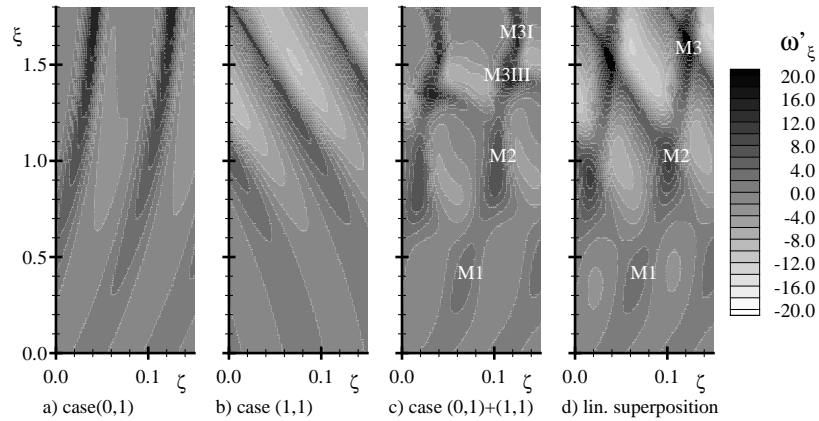


Figure 3 Component w'_ξ of the perturbation vorticity in the plane $y = 0.85 \cdot 10^{-2} \approx 0.25 \cdot \delta$ for the different simulation cases and for the linear superposition of the perturbation fields from cases $(0, 1)$ and $(1, 1)$ (fig. d). The primary main vortices rotate clockwise when looking downstream and have negative w'_ξ values. The ξ -axis spans an angle of 45° with the x -axis and is nearly parallel to the local edge velocity. The origin of the rotated system lies in $x = 2.13, z = 0.07$.

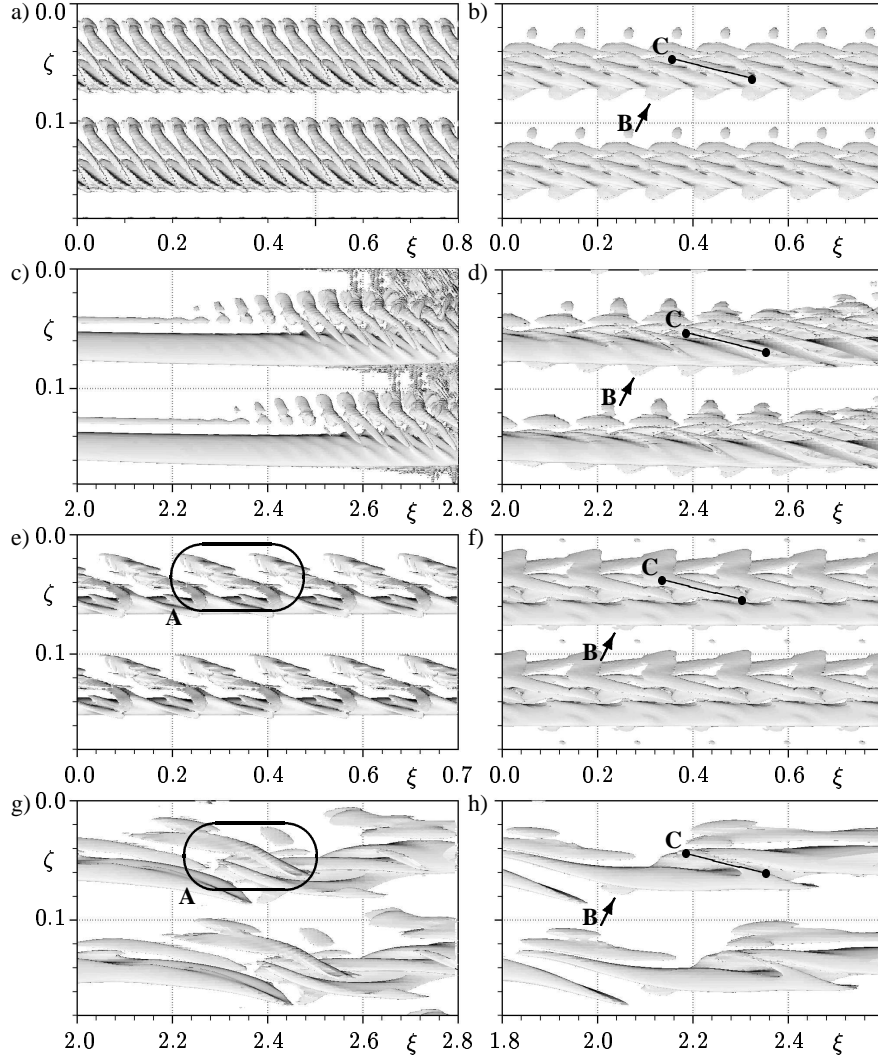


Figure 4 Visualization (top view, two spanwise wavelengths) of secondary structures by means of λ_2 -isosurfaces: a) superposition of the primary state from case $(0, 1)$ ($x = 3.32$, $\xi \approx 1.58$) and eigenfunctions for mode I ($\beta_\psi = 134$, $\omega \approx 120$, maximal amplitude of the u_ξ component of the eigenfunction $A'' = 0.1 \cdot u_{bse}$); b) as a) for mode III ($\beta_\psi = 62$, $\omega \approx 30$, $A'' = 0.1 \cdot u_{bse}$); c) DNS for case $(0, 1)$ under additional excitation of mode I ($\omega = 120$) in the saturation region; d) as c) for mode III ($\omega = 30$); e) superposition of primary state from case $(0, 1) + (1, 1)$ ($x = 3.42$, $\xi \approx 1.58$, $t = 0.4 \cdot T$) and eigenfunctions for mode I ($\beta_\psi = 40$, $\omega \approx 30$, $A'' = 0.25 \cdot u_{bse}$); f) superposition of primary state from case $(0, 1) + (1, 1)$ ($x = 3.61$, $\xi \approx 2.11$, $t = 0.44 \cdot T$) and mode III ($\beta_\psi = 40$, $\omega \approx 20$, $A'' = 0.25 \cdot u_{bse}$); g) mode-I structure from DNS for case $(0, 1) + (1, 1)$ ($t = 0.48 \cdot T$); h) mode-III structure from DNS for case $(0, 1) + (1, 1)$ ($t = 0.26 \cdot T$). Same letters indicate corresponding structures. See caption of fig. 3 for definition of the reference system.

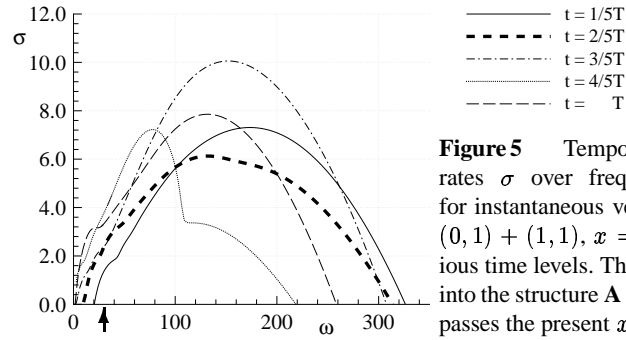


Figure 5 Temporal SLST amplification rates σ over frequency for mode I and for instantaneous velocity profiles from case $(0, 1) + (1, 1)$, $x = 3.42$, $\xi \approx 1.58$, at various time levels. The perturbation developing into the structure **A** of fig. 4g ($\omega \approx 30$, arrow) passes the present x -position for $t = 2/5T$.

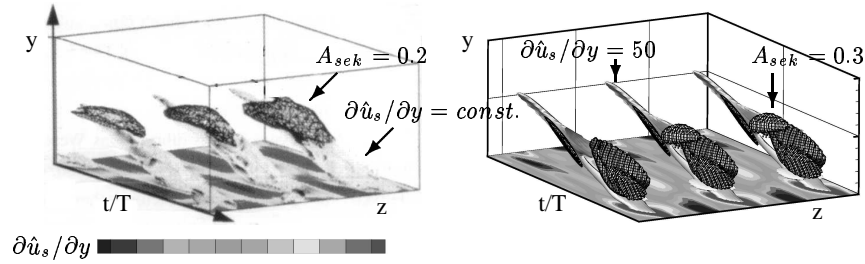


Figure 6 Comparison of experimental [5] and DNS results for case $(0, 1) + (1, 1)$: a) experiment [5]; b) DNS for $x = 3.63$. \hat{u}_s is the time-dependent component of the downstream velocity: $\hat{u}_s = u_s - \langle u_s \rangle$; $\partial \hat{u}_s / \partial y$ is the wall-normal shear of the unsteady part of the fbw. According to [5] A_{sek} is a normalization of the second time derivative of u_s , and is large in regions presenting high frequency perturbations.

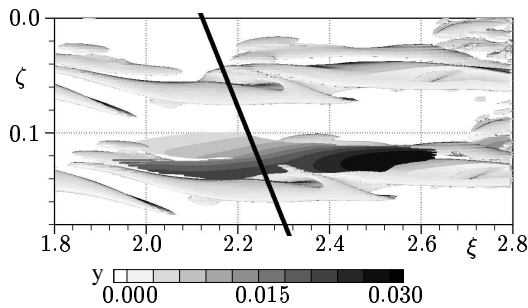


Figure 7 Spatial visualization for case $(0, 1) + (1, 1)$, $t = 0.52 \cdot T$, of the isosurfaces $\partial \hat{u}_s / \partial y = 50.0$ from fig. 6b (shaded, the color shows the distance of the isosurface points from the wall) and of λ_2 -isosurfaces (not shaded). The thick line shows the section plane, data for fig. 6b originate from.